Element-specific electronic structure and magnetic properties of an epitaxial $Ni_{51.6}Mn_{32.9}Sn_{15.5}$ thin film at the austenite-martensite transition

B. Krumme,[1] A. Auge,[2] H. C. Herper,[3] I. Opahle,[4] D. Klar,[1] N. Teichert,[2] L. Joly,[5] P. Ohresser,[6] J. Landers,[1] J. P. Kappler,[5] P. Entel,[1] A. Hütten,[2] and H. Wende[1,*]

[1]*Faculty of Physics and Center for Nanointegration Duisburg-Essen (CENIDE), University of Duisburg-Essen, Lotharstraße 1, D-47048 Duisburg, Germany*

[2]*Center for Spinelectronic Materials and Devices, Department of Physics, Bielefeld University, Post Office Box 100131, D-33501 Bielefeld, Germany*

[3]*Department of Physics and Astronomy, Uppsala University, Box 516, 75120 Uppsala, Sweden*

[4]*ICAMS, Ruhr-Universität Bochum, D-44801 Bochum, Germany*

[5]*Université de Strasbourg, Institut de Physique et de Chimie des Materiaux de Strasbourg, Campus de Cronenbourg, 23 Rue du Loess, 67034 Strasbourg Cedex 2, France*

[6]*Synchrotron SOLEIL, L'Orme des Merisiers, Saint-Aubin BP 48, 91192 Gif-sur-Yvette, France*

(Received 11 March 2015; published 11 June 2015)

An austenite-martensite transition was observed in a 100-nm-thick $Ni_{51.6}Mn_{32.9}Sn_{15.5}$ film by temperature-dependent resistivity and magnetization measurements, revealing a martensite starting temperature of $M_S \approx 260$ K. The influence of the structural phase transition on the electronic structure and the magnetic properties was studied element specifically employing temperature-dependent x-ray-absorption spectroscopy and x-ray magnetic circular dichroism. In addition, density functional theory calculations have been performed to study the electronic and magnetic properties of both phases. It is shown that off-stoichiometric Ni-Mn-Sn alloys can exhibit a substantial magnetocrystalline anisotropy energy in the martensite phase. For Mn a change of the electronic structure and a strong increase of the ratio of orbital to spin magnetic moment m_l/m_S can be observed, whereas for Ni nearly no changes occur. Applying an external magnetic field of $B = 3$ T reverses the change of the electronic structure of Mn and reduces the ratio of m_l/m_S from 13.5 to ≈1 % indicating a field-induced reverse martensitic transition.

DOI: 10.1103/PhysRevB.91.214417 PACS number(s): 71.20.Be, 78.70.Dm, 71.15.Mb, 75.20.En

I. INTRODUCTION

Recently, ferromagnetic shape memory alloys, such as Ni_2MnGa [1,2], exhibit potential for applications as actuators, since it is possible to induce large strain (up to 10%) by applying an external magnetic field in the martensite phase [3,4]. Such compounds exhibit a structural phase transition from a high-temperature cubic austenite phase into a tetragonally distorted (or modulated orthorhombic/monoclinic) phase at low temperature. One group of materials that exhibit this behavior is that of the Mn-rich $Ni_2Mn_{1+x}Sn_{1-x}$ compounds like $Ni_{50}Mn_{35}Sn_{15}$ [5]. The structural phase transition is accompanied by a strong change of the magnetization or the resistivity [6].

Since the transition temperatures of the structural and magnetic phase transition depend on the number of valence electrons per atom in the unit cell, the Mn-rich compounds provide the possibility to engineer the transition temperatures by changing the content of Mn and Sn [5].

However, to get a complete understanding of the effects causing the structural phase transition the microscopic origin of the martensite-austenite transition needs to be studied. Therefore, we present an element-specific investigation of the temperature dependence of the electronic structure and the magnetic properties of Ni and Mn in a $Ni_{51.6}Mn_{32.9}Sn_{15.5}$ Heusler compound. Additionally, the influence of high magnetic fields applied in the martensite phase on the above-mentioned properties will be discussed.

II. EXPERIMENTAL ASPECTS

A 100-nm-thick $Ni_2Mn_{1+x}Sn_{1-x}$ film was grown on a MgO(100) substrate using DC/RF magnetron sputtering in a UHV system with a base pressure of $p \leqslant 1 \times 10^{-9}$ mbar. The three elements were sputtered from elemental sources with a total growth rate of 3.1 Å/s. During the deposition the substrate temperature was kept at $T = 880$ K and the substrate was rotated with approximately ten rounds per minute to obtain a homogeneous film. Finally, the film was capped with a 2-nm-thick MgO layer to prevent the sample from oxidation. E-beam evaporated MgO capping layers do not cause any oxidation with underlying Heusler-like thin films as was reported elsewhere [7]. The stoichiometry of the sample was determined by x-ray fluorescence: $Ni_{51.6}Mn_{32.9}Sn_{15.5}$. Bulk structural and magnetic properties were studied using x-ray diffraction (XRD) with Cu K_α radiation and superconducting quantum interference device (SQUID) magnetometry; the latter one was done field as well as temperature dependent.

In order to study the electronic structure as well as the magnetic properties element specifically, x-ray-absorption spectroscopy (XAS) and x-ray magnetic circular dichroism (XMCD) measurements were performed in the surface-sensitive total electron yield (TEY) mode at the DEIMOS beamline at the French synchrotron radiation facility SOLEIL in Paris, France. The dichroic signal was obtained by switching

*Corresponding author: heiko.wende@uni-due.de

the circular polarization of the x-ray photons at a constant applied magnetic field. A sum rule analysis following Thole and Carra *et al.* was done to determine the spin and orbital resolved magnetic moments of Ni and Mn [8,9]. To correct the sum rule of the spin magnetic moment for Mn, a spin correction factor (SCF) of 1.5 was used to account for the jj mixing of the initial $2p_{3/2}$ and $2p_{1/2}$ states [10].

III. THEORETICAL DETAILS

The electronic and magnetic structure of the off-stoichiometric Heusler alloy were calculated from density functional theory (DFT) using the fully relativistic Green's-functions approach SPR-KKR [11] and the generalized gradient approximation in the formulation of Perdew, Burke, and Ernzerhof (PBE) [12]. Calculations were performed for $Ni_{51.6}Mn_{32.9}Sn_{15.5}$ with the excess Mn atoms located on the Sn sublattice. The tiny amount of excess Ni has been placed on the Mn sublattice. Disorder is described within the coherent potential approximation whereby $L2_1$ order was assumed for the austenite phase and a tetragonally distorted $L1_0$ structure with ratio between in-plane and out-of-plane lattice constant $c/a = 1.2$ has been used for the martensite phase. The cubic lattice constant amounts to $a = 5.98$ Å. Both, the c/a ratio and the a have been taken from supercell calculations for $Ni_8Mn_5Sn_3$ and $Ni_8Mn_6Sn_2$ and are comparable to the results of Sokolovskiy *et al.* within the local density approximation [13]. The scattering path operator was used to determine the XAS and XMCD spectra at the Ni and Mn $L_{2,3}$ edges in the martensite and the austenite phase [11].

For the calculation of the magnetocrystalline anisotropy energy (MAE) as a function of the c/a ratio we used the relativistic version of the full potential local orbital code [14,15] (version 9.01-35). In this scheme the four-component Kohn-Sham-Dirac equation, which includes spin-orbit coupling up to all orders, is solved self-consistently. The stoichiometry of the $Ni_{51.6}Mn_{32.9}Sn_{15.5}$ film was approximated with an ordered $Ni_8Mn_5Sn_3$ ($Ni_{50}Mn_{31.3}Sn_{18.8}$) supercell with antiferromagnetic alignment of the additional Mn atom on the Sn sublattice with respect to the remaining Mn atoms. For the MAE calculation, the local spin-density approximation in the parametrization of Perdew and Wang [16] was employed. For the k-space integration 8000 points in the full Brillouin zone were used. In the variation of the c/a ratio the volume was kept fixed corresponding to a lattice parameter $a = 6.01$Å in the cubic $L2_1$ phase.

IV. RESULTS

A. Characterization

The bulk crystal structure of the 100-nm-thick $Ni_{51.6}Mn_{32.9}Sn_{15.5}$ film was characterized by means of XRD. A Θ-2Θ scan [see Fig. 1(a)] shows a (200) B2 superlattice reflection ($2\Theta = 29.88°$) and a (400) fundamental reflection ($2\Theta = 62.08°$) indicating B2 type ordering of the film with a lattice constant of $a = 5.980 \pm 0.001$Å. Also an additional peak **S** ($2\Theta = 50.13°$) can be observed, possibly due to a small segregation of NiMn. At 39 and 83° there are MgO(200) and MgO(400) reflections from the remaining Cu K_β radiation visible. A pole figure scan reveals the (111) reflection of the Ni-Mn-Sn compound [see Fig. 1(b)] at 54.7° indicating that

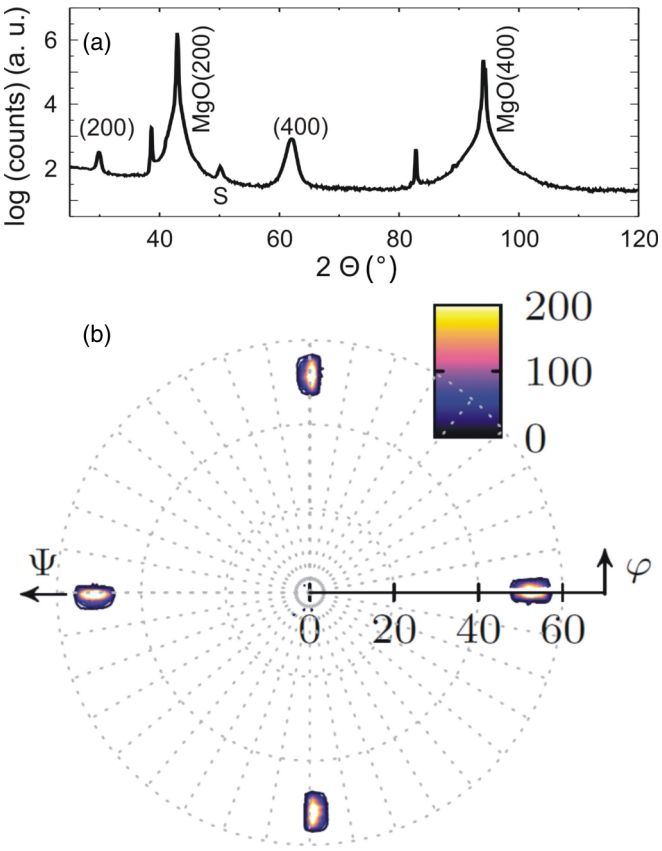

FIG. 1. (Color online) (a) θ-2θ scan of the 100-nm-thick $Ni_{51.6}Mn_{32.9}Sn_{15.5}$ film on MgO(100) measured in the cubic austenite phase. (b) Pole figure scan of the (111) reflection ($\varphi = 0$ corresponds to the [010] direction of the MgO substrate).

the film exhibits partial $L2_1$ ordering and epitaxial growth with the relation MgO(100)[010]‖NiMnSn(100)[011].

In order to study the structural phase transition, the temperature-dependent magnetization was measured in an applied magnetic field of $B = 5$ mT. Figure 2(a) yields a Curie temperature of $T_C = (320 \pm 5)$ K and a martensite starting temperature of $M_S = (260 \pm 5)$ K, being in good agreement with the temperature-dependent magnetization of bulk $Ni_2Mn_{1.4}Sn_{0.6}$ from Krenke *et al.* [5]. Again, we observe the typical thermal hysteresis upon cooling and heating the sample.

Also shown in Fig. 2(b) are normalized magnetic hysteresis curves of the austenite (red circles) and the martensite phase (black squares). For the austenite phase we observe a very narrow hysteresis curve with a small coercive field of $H_{C,\mathrm{Aust}} = 2$ mT, whereas the hysteresis of the martensite phase becomes much broader yielding a coercive field of $H_{C,\mathrm{Aust}} = 10$ mT. Such a change of the shape of the magnetic hysteresis as well as the increase of the coercive field were also found in literature for Ni_2MnGa [17]. These changes can be explained by the structural phase transition, since it is accompanied by a substantial change of the magnetic anisotropy (see Sec. V).

B. X-ray-absorption experiments

In order to investigate the influence of the structural phase transition on the element-specific electronic structure and

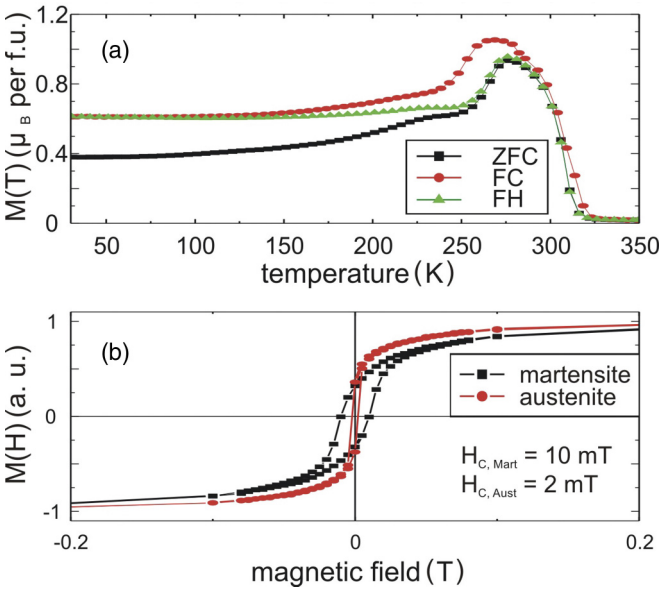

FIG. 2. (Color online) (a) Zero-field cooled (ZFC), field cooled (FC), and field heated (FH) magnetization curves. (b) Normalized magnetic hysteresis curves of the austenite (red circles) and the martensite (black squares) phase. For the magnetization measurements the magnetic field was applied parallel to the film plane.

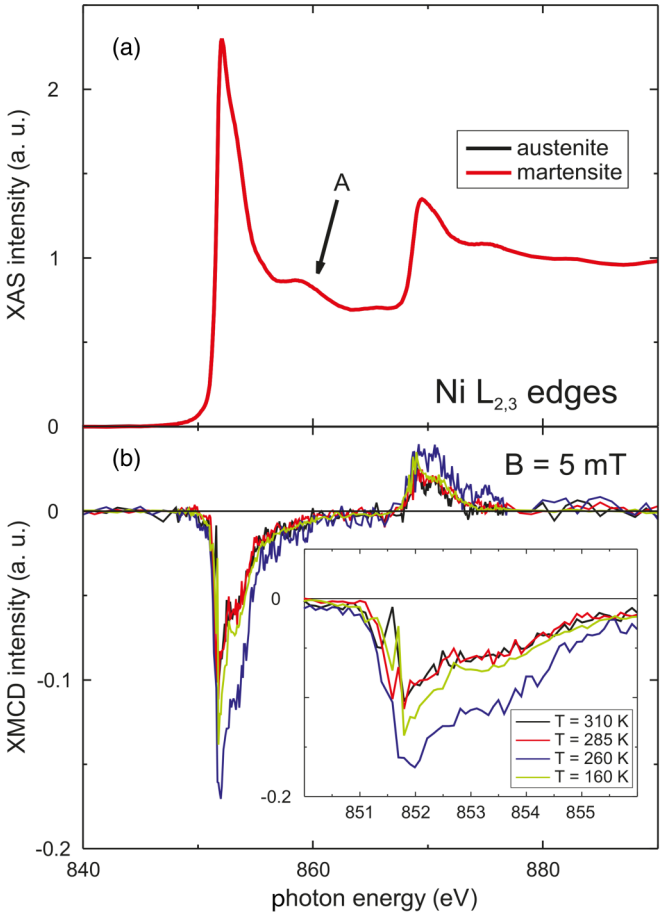

FIG. 3. (Color online) (a) XAS of the austenite (black curve) and martensite phase (red curve). (b) Temperature-dependent XMCD signal measured at the Ni $L_{2,3}$ edges.

magnetic properties, temperature-dependent measurements of the near-edge x-ray absorption fine-structure NEXAFS and XMCD were done at the Ni (Fig. 3) and Mn (Fig. 4) $L_{2,3}$ edges. Figure 3(a) shows the electronic structure of Ni in the austenite (black curve) as well as the martensite phase (red curve). For both structural phases we observe a well-defined satellite peak **A** about 6.5 eV above the L_3 maximum, which was also reported for Ni in Ni_2MnGa [18]. In this work the satellite structure was found to vanish when the crystal structure changes from cubic austenite to tetragonally distorted martensite. However, almost no change of the electronic structure of Ni at the structural phase transition has been observed in our experiment. As expected from the temperature dependence of the bulk magnetization from SQUID [Fig. 2(a)] the XMCD signal of the induced Ni moments [Fig. 3(b)] increases when decreasing the temperature from $T = 310$ to 260 K, and decreases at $T = 160$ K. All the Ni XMCD signals exhibit fine structures at the L_3 and the L_2 edge, similar to the ones observed for Ni in Ni_2MnGa [18].

In contrast to Ni, the structural phase transition leads to a small increase of the XAS signal at the Mn $L_{2,3}$ edges in the martensite phase [Fig. 4(a), inset]. Despite that, no changes of the spectral shape can be observed. Both the XAS as well as the XMCD signal are comparable with one obtained for Mn in Co_2MnSi [19]. The trend of the temperature-dependent XMCD signal of Mn is the same as discussed above for Ni.

A sum rule analysis following Thole and Carra *et al.* [8,9] was performed in order to study the temperature dependence of the orbital and spin magnetic moments of Ni and Mn. The number of unoccupied d states of Ni and Mn was taken from DFT calculations using the SPR-KKR package, which were performed within this work, taking into account a stoichiometry of $Ni_{51.6}Mn_{32.9}Sn_{15.5}$: $n_{\mathrm{Ni,\,Aust}} = 1.31$, $n_{\mathrm{Ni,\,Mart}} = 1.32$, $n_{\mathrm{Mn,\,Aust}} = 4.52$, and $n_{\mathrm{Mn,\,Mart}} = 4.49$.

The results of a sum rule analysis for Ni and Mn are shown in Figs. 5(a)–5(d). The temperature dependence of the spin and orbital resolved magnetic moments (red squares) are compared to scaled temperature-dependent magnetization curves measured by SQUID (black curve). In the case of the spin magnetic moment of Mn, a constant SCF of 1.5 for all temperatures was assumed. Therefore, the determined spin magnetic moment of Mn is an effective moment, since it is difficult to estimate the influence of the structural phase on the mixing of the initial $2p_{3/2}$ and $2p_{1/2}$ electronic states and, therefore, on the spin correction factor.

The temperature dependence of the element-specific magnetic moments m_S(Ni) [Fig. 5(a)], m_l(Ni) [Fig. 5(b)], and $m_{S,\mathrm{eff}}$(Mn) resembles the behavior of the bulk magnetization quite well. However, the orbital magnetic moment of Mn m_l(Mn) shows a different behavior. Here, a strong increase can be observed with decreasing temperature. This becomes more obvious taking a closer look at the ratio of orbital to spin magnetic moment m_l/m_S (Fig. 8, black squares) of Ni and Mn. For Ni, m_l/m_S remains almost constant at a high value of roughly 31%, whereas for Mn an increase of m_l/m_S from $\approx 5\%$ in the austenite phase to 13.5% in the martensite phase is being observed. The increasing ratio m_l/m_S of Mn

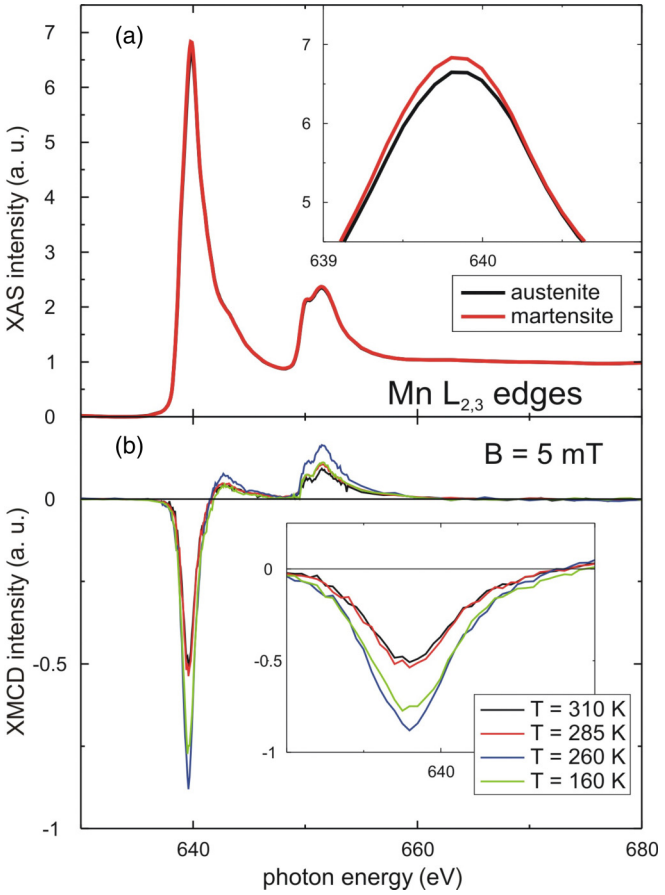

FIG. 4. (Color online) (a) XAS of the austenite (black curve) and martensite phase (red curve). (b) Temperature-dependent XMCD signal measured at the Mn $L_{2,3}$ edges.

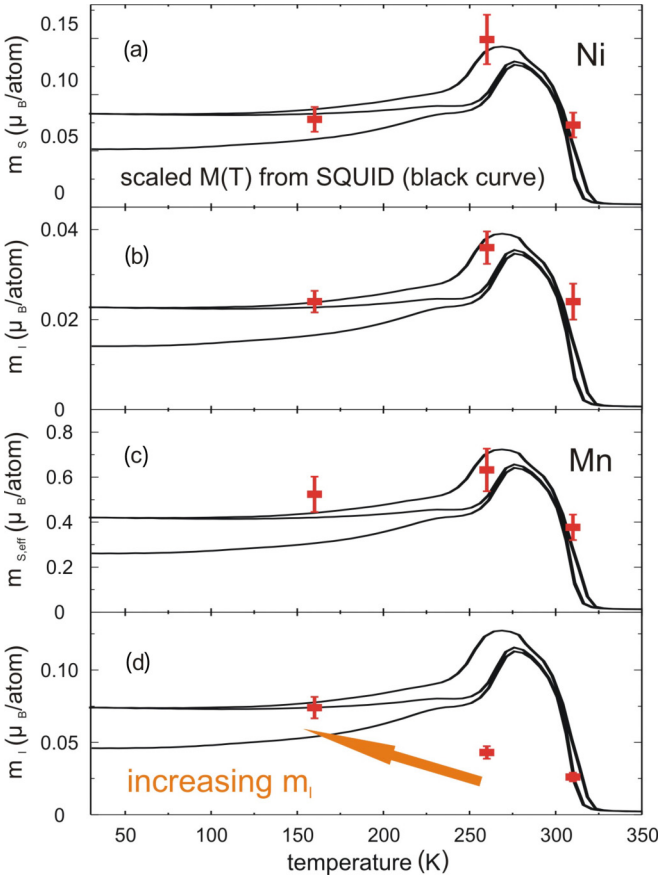

FIG. 5. (Color online) Temperature dependence of the spin and orbital resolved magnetic moments of Ni (a, b) and Mn (c, d) determined by a sum rule analysis. A scaled M(T) curve from SQUID measurements (black curve) is plotted for a comparison with the bulk M(T) behavior.

can be related to the structural phase transition from the cubic $L2_1$ phase to a distorted martensite phase leading to a diminished quenching of the orbital magnetic moment. A similar effect was observed in FePt nanoparticles, where a tetragonal distortion leads to an increase of the ratio of m_l/m_S [20].

Summing up the spin and orbital magnetic moments from the XMCD measurements, we obtain an overall magnetization of $m_{\mathrm{XMCD}} = (1.26 \pm 0.19)\mu_B$ per formula unit at $T = 260$ K. This is in good agreement with SQUID measurements, which have been performed in parallel, yielding a magnetization of $m_{\mathrm{SQUID}} = (1.05 \pm 0.05)\mu_B$ per formula unit at $T = 265$ K.

C. Influence of high magnetic fields

Since it is known from literature [3,4] that it is possible to induce large strain by applying an external magnetic field in the martensite phase, the influence of high magnetic fields up to $B = 3$ T on the electronic structure of Mn was studied. In Fig. 6(a) the comparison of the Mn XAS of the austenite phase (black curve), the martensite phase (red curve), and the martensite phase with an applied magnetic field of $B = 3$ T is shown. As already discussed, the structural phase transition is accompanied by an increase of the x-ray-absorption intensity in the low-temperature martensite phase. But the application of an external magnetic field of $B = 3$ T leads to a reduction of the absorption intensity back to the value observed for the austenite phase (Fig. 6, inset). The change of the electronic structure can be an indication of a field-induced reverse martensitic transition (FIRMT) [21], indicating that the magnetic field pushed the system from the martensite back into the austenite phase. The XMCD signal of Mn was measured for magnetic fields of $B = 1.5$ and 3 T [Fig. 6(b)]. Here, we observe small differences of the XMCD intensity at the $L_{2,3}$ edges and in between. Since the sample should be magnetically saturated at an external field of $B = 0.2$ T for both phases [see Fig. 2(b)], we assume the small differences of the XMCD signal to be caused by the influence of the magnetic field on the crystal structure and, therefore, on the electronic hybridization. The changes of the XMCD can be related to two effects, the first being the result of a spin-dependent reoccupation of electronic states induced by a structural phase transition from a distorted phase to a cubic one as it was theoretically predicted for Ni_2MnGa [22]. Secondly, the change of the XMCD signal could be connected to a change of the ratio of m_l/m_S. Additionally, larger changes of the electronic structure are observed at the Ni $L_{2,3}$ edges (Fig. 7). In this figure a comparison of the electronic structure of the Ni $L_{2,3}$ edges is shown for the austenite as well as the martensite phase with a small applied magnetic field of $B = 5$ mT and for the

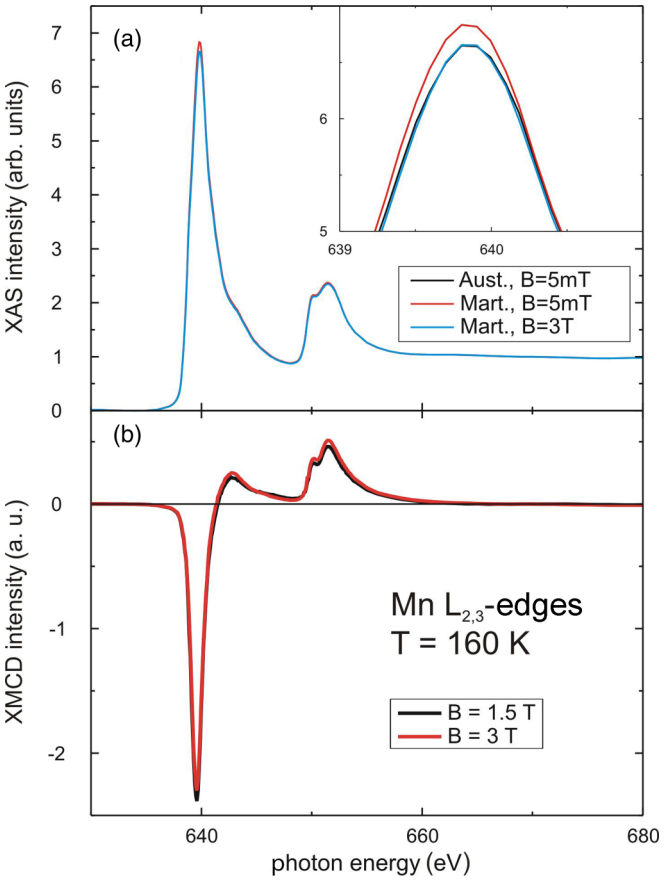

FIG. 6. (Color online) (a) XAS of the Mn $L_{2,3}$ edges in the austenite (black curve) and martensite phase (red curve) in an applied magnetic field of $B = 5$ mT compared to the XAS of the martensite phase with an applied magnetic field of $B = 3$ T (blue curve). (b) XMCD signal of Mn in the martensite phase with an applied magnetic field of $B = 1.5$ T (black curve) and $B = 3$ T (red curve).

martensitic phase with an applied magnetic field of $B = 3$ T. As discussed before, almost no change can be observed for the electronic structure of Ni at the structural phase transition. But, after the application of a magnetic field of $B = 3$ T, the intensity of the XAS signal slightly decreases, which again is a hint to a FIRMT as stated before for the behavior of the electronic structure of Mn.

The dependence of the ratio m_l/m_S on the magnetic field is shown in Fig. 8 for $T = 160$ K (blue squares). For both Mn and Ni, a decrease of m_l/m_S with increasing magnetic field is observed. In case of Mn, the application of a magnetic field of $B = 1.5$ T leads to a reduction of m_l/m_S from 13.5 to 4.4%, increasing the magnetic field to $B = 3$ T yields a larger reduction of m_l/m_S resulting in $m_l/m_S \approx 1\%$. Simultaneously, m_l/m_S of Ni decreases from initially 31 to 16%, when a magnetic field of $B = 3$ T is applied. The fact that the ratio m_l/m_S can be reduced to a value smaller than observed in the austenite phase in a small external magnetic field leads to the conclusion that the film was already distorted in the austenite phase. Since our measurements were done in the surface sensitive TEY mode, this distortion could have been induced by the MgO capping layer. A similar effect was observed for MgO-capped Ni_2MnGa, where the structural

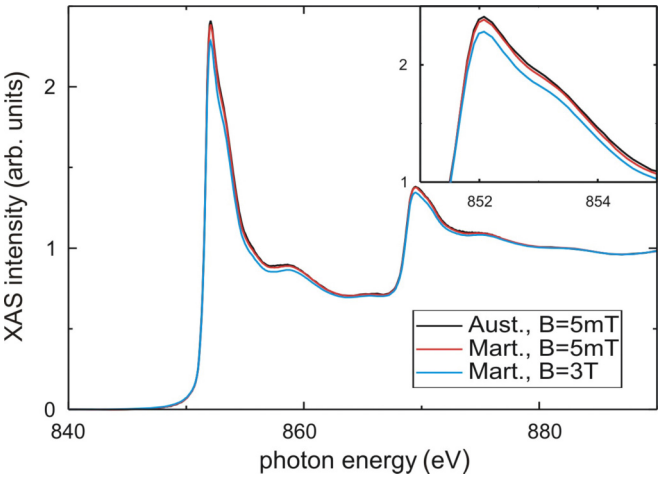

FIG. 7. (Color online) XAS of the Ni $L_{2,3}$ edges in the austenite (black curve) and martensite phase (red curve) in an applied magnetic field of $B = 5$ mT compared to the XAS of the martensite phase with an applied magnetic field of $B = 3$ T (blue curve).

phase transition was completely suppressed by the capping layer [23].

V. THEORETICAL CALCULATIONS

In order to distinguish between field and temperature driven changes in the XAS we have calculated the spectra for the $L2_1$ and $L1_0$ structure of $Ni_{51.6}Mn_{32.9}Sn_{15.5}$. Regardless of the structure the system prefers ferrimagnetic order, i.e., the Mn atoms on the Mn and Sn sublattice are aligned antiparallel (see Fig. 9). The resulting spin moment is 1.47 μ_B (1.46 μ_B) for the $L2_1$ ($L1_0$) structure (see Table I), which agrees qualitatively with the experimentally observed trend. However, the reduction of the Mn spin moment is much smaller compared to the experiment and the $\bar{m}_l/\bar{m}_s$ ratio is quite small in both phases. On the one hand this may be related to a typical underestimation of orbital moments and (slight) overestimation of spin moments in GGA. On the other hand

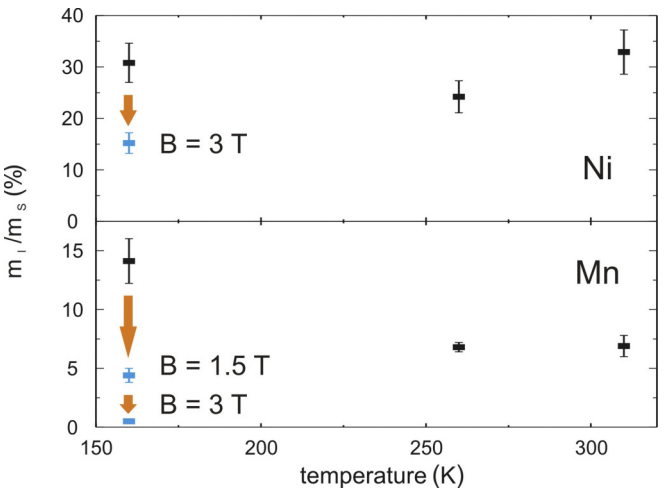

FIG. 8. (Color online) Temperature-dependent (black squares) and field-dependent (blue squares) ratio of orbital to spin magnetic moment m_l/m_S of Ni and Mn.

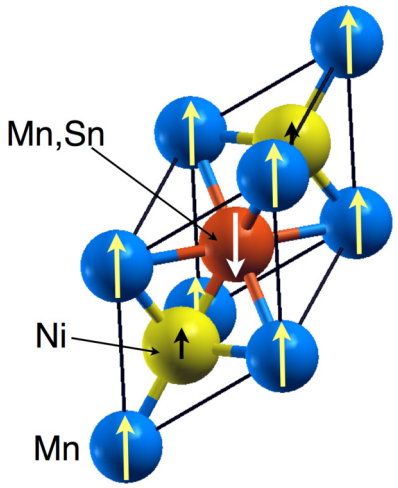

FIG. 9. (Color online) Sketch of the calculated spin structure of $Ni_{51.6}Mn_{32.9}Sn_{15.5}$ in the orthorhombic unit cell. The magnetic moments of Mn on the Mn sublattice and excess Mn atoms on the Sn sublattice are aligned antiparallel. Sn moments are not shown.

the net spin moments $\bar{m}_s$ are by a factor of 1.5 larger than the measured ones, which is an indication of a higher structural order as in experiment.

The spin moments of Ni do not follow the experimental trend. On the contrary the average spin moment of Ni in the tetragonal phase amounts to 0.21 μ_B and is therefore slightly larger than in the cubic phase (0.16 μ_B) (see Table I). Since the Ni moments are induced moments they are always oriented in direction of the net magnetization and changes in the local coordination have strong impact on the result. Here, we have assumed perfect $L2_1$ and $L1_0$ order, whereas in experiment also partially B2 order is observed (see Fig. 1). However, the ratio between the average orbital and spin moments $\bar{m}_l/\bar{m}_s$ of Ni is mainly unaffected by the structural transition, which corresponds to the experimental observations (see Fig. 8).

The calculated XAS of the $L2_1$ and the $L1_0$ phase are shown in Fig. 10 together with the corresponding XMCD spectra. In agreement with the experimental findings without magnetic field (see Fig. 4) the XMCD of the martensitic phase is reduced compared to the XMCD of the austenite phase. The XAS remains mostly unchanged, i.e., differences lie within the line width. Only the shoulder at approximately 5 eV slightly decreases when symmetry is reduced. The occurrence of the shoulder which is experimentally observed [see Fig. 3(a)] is related to hybridization effects of Sn d states with Ni and Mn

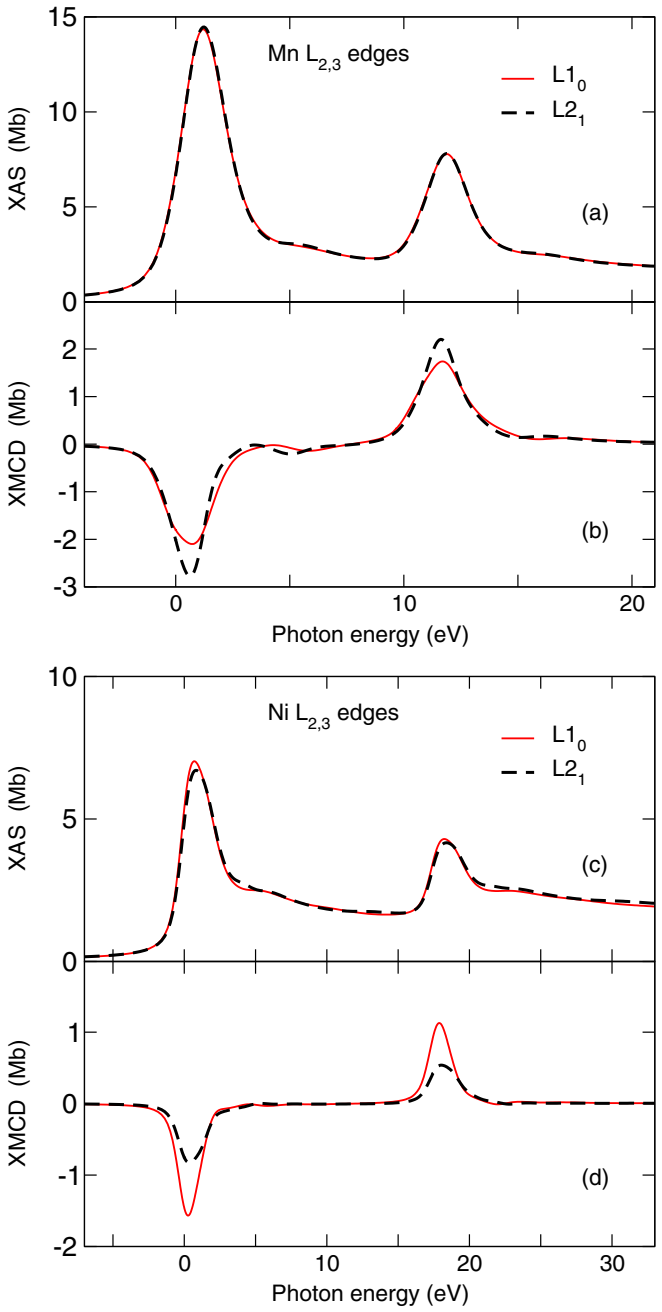

FIG. 10. (Color online) Calculated XAS of Mn (a) and Ni (c) in $Ni_{51.6}Mn_{32.9}Sn_{15.5}$ together with the corresponding XMCD (b, d, respectively). Dashed lines denote the spectra of the cubic phase and full lines mark the results for the $L1_0$ ordered phase.

TABLE I. Calculated spin moment (m_s) for Ni and Mn atoms in $Ni_{51.6}Mn_{32.9}Sn_{15.5}$. The value gives the magnetic moment of the excess Ni atoms (Mn atoms) on the Mn sublattice (Sn sublattice). $\bar{m}$ denotes the average spin moment of a species.

Structure	Mn (μ_B)			Ni (μ_B)		
	m_s	$\bar{m}$	$\bar{m}_l/\bar{m}_s$	m_s	$\bar{m}$	$\bar{m}_l/\bar{m}_s$
$L2_1$ AF	3.70 (−4.02)	1.47	0.010	0.16 (0.25)	0.16	0.083
$L1_0$ AF	3.67 (−3.98)	1.46	0.012	0.21 (0.24)	0.20	0.094
$L1_0$ FM	3.68 (3.95)	3.76	0.005	0.43 (0.33)	0.43	0.115

d states as a result of our DFT calculations. These features are reduced in the tetragonal phase (see Fig. 10). A similar shoulder is observed for Ni, which seems to be more sensitive to structural changes (see Fig. 10). However, no temperature dependence of the shoulder feature is measured through the austenite-martensite transition. This feature can be explained by the MgO capping layer lattice constraints on the Heusler film resulting in a residual austenite interface region near the MgO-Heusler film interface. Similar observations are reported

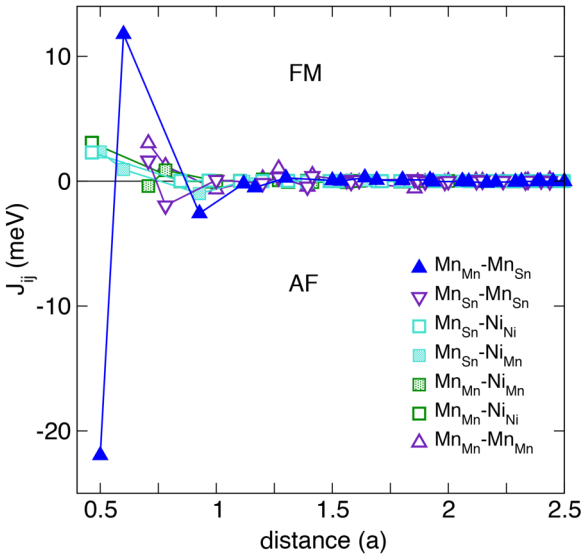

FIG. 11. (Color online) Calculated magnetic exchange parameters J_{ij} of $Ni_{51.6}Mn_{32.9}Sn_{15.5}$ depending on the distance between atoms in units of the lattice constant a.

for ferromagnetic shape memory Heusler alloy thin films grown on MgO substrates [24].

In case of FM order the size of the individual Mn moments remains mostly unchanged, but now moments on different sublattices are aligned parallel to each other. The Ni moments increase such that the average spin moments become larger by a factor of 2.6 and the m_l/m_S ratio for Mn becomes smaller in case of the $L1_0$ structure, which contradicts the experimental findings (see Table I). In addition a broader XMCD signal is expected from theoretical calculations (not shown here). This is not observed if a magnetic field is applied to the martensitic phase (see Fig. 6). Furthermore, a strong antiferromagnetic exchange coupling exists between Mn atoms on the Mn and Sn sublattice. The nearest-neighbor coupling exceeds -20 meV (see Fig. 11). Hence, the experimentally applied field of 3 T is not sufficient to overcome the AF coupling.

Figure 12 shows the calculated magnetocrystalline anisotropy energy (MAE) of $Ni_8Mn_5Sn_3$ as a function of the c/a ratio. Similar to Ni_2MnGa [25] a nearly linear dependence of the MAE on the c/a ratio with a change of sign at $c/a = 1$ is found in the vicinity of the cubic $L2_1$ phase. For $c/a > 1$ the [001] direction is the hard axis while the [100] and [110] directions have the lowest energy, resulting in an easy plane anisotropy. The in-plane anisotropy between [100] and [110] directions is in the range of a few μeV/f.u. or less, which is below the accuracy of the present calculations. The [111] and [011] directions (not shown) are intermediate. At $c/a = 1.2$ a sizable absolute value of the MAE of 0.42 meV/f.u. is found. Compared to Ni_2MnGa [25] with an MAE of 0.7 meV/f.u. this value is slightly reduced. The MAE in the cubic $L2_1$ phase is more than two orders of magnitude smaller, in agreement with the experimentally observed narrow hysteresis and the small coercive field (Fig. 2).

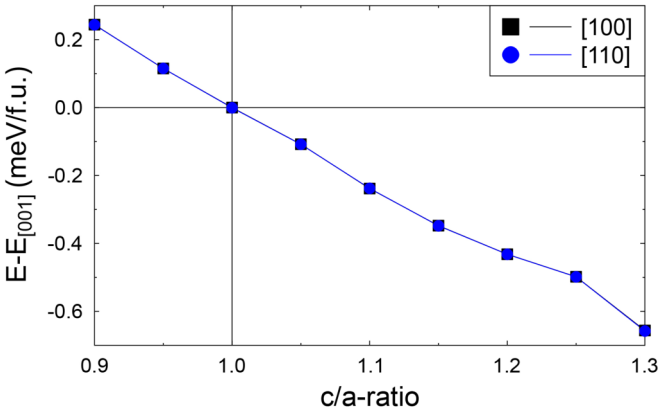

FIG. 12. (Color online) MAE of $Ni_2Mn_{1.25}Sn_{0.75}$ ($Ni_8Mn_5Sn_3$) in dependence of the c/a ratio. Shown is the energy difference between the easy axes [100]/[110] and the hard axis [001].

VI. SUMMARY

In summary, we studied the temperature dependence of the electronic structure and the magnetic properties of $Ni_{51.6}Mn_{32.9}Sn_{15.5}$ element specifically by XAS, XMCD, and DFT calculations. For Mn we observe a small increase of the x-ray-absorption intensity when the sample undergoes the structural phase transition from austenite to martensite. From DFT calculations it turned out that the magnetic structure in both phases is ferrimagnetic, i.e., the spin moments of Mn atoms on different sublattices are aligned antiparallel. Hence, the net spin moment of Mn is much smaller than in the stoichiometric Ni_2MnSn compound [26]. Further, it is shown that also off-stoichiometric Ni-Mn-Sn Heusler alloys close to the film composition can exhibit a large MAE in the martensite phase, while it is small in the cubic austenite phase, in agreement with the experimentally observed changes in the magnetic hysteresis. In experiment the change of the electronic structure of Mn is accompanied by a rather large increase of the ratio m_l/m_S from 5–6% in the austenite phase to 13.5% in the orthorhombic martensite one. In contrast, for Ni no changes are found within the sensitivity of our measurements. By applying a large magnetic field of up to $B = 3$ T, m_l/m_S strongly reduces for Mn and Ni, indicating a FIRMT. Theoretical investigations of XAS and magnetic exchange parameters contradict a transformation from AF to FM in magnetic fields up to 3 T. At $B = 3$ T, m_l/m_S becomes even smaller than initially observed in the austenite phase, leading to the conclusion that the MgO capping layer caused a distortion of the top NiMnSn layers, which could be reversed by the application of a high magnetic field.

ACKNOWLEDGMENTS

We gratefully acknowledge help during our beam times by SOLEIL staff. This work is supported by Deutsche Forschungsgemeinschaft (SFB 491 and SPP 1599).

[1] H. Hosoda, K. Wakashima, T. Sugimoto, and S. Miyazaki, Mater. Trans. **43**, 852 (2002).

[2] P. J. Webster, K. R. A. Ziebeck, S. L. Town, and M. S. Peak, Philosophical Magazine **49**, 295 (1984).

[3] K. Ullakko, J. K. Huang, C. Kantner, R. C. O'Handley, and V. V. Kokorin, Appl. Phys. Lett. **69**, 1966 (1996).
[4] K. Ullakko, J. K. Huang, V. V. Kokorin, and R. C. O'Handley, Scr. Mater. **36**, 1133 (1997).
[5] T. Krenke, M. Acet, E. F. Wassermann, X. Moya, L. Mañosa, and A. Planes, Phys. Rev. B **72**, 014412 (2005).
[6] N. Teichert, A. Auge, E. Yüzüak, I. Dincer, Y. Elerman, B. Krumme, H. Wende, O. Yildirim, K. Potzger, and A. Hütten, Acta Mater. **86**, 279 (2015).
[7] M. Glas, C. Sterwerf, J. M. Schmalhorst, D. Ebke, C. Jenkins, E. Arenholz, and G. Reiss, J. Appl. Phys. **114**, 183910 (2013).
[8] B. T. Thole, P. Carra, F. Sette, and G. van der Laan, Phys. Rev. Lett. **68**, 1943 (1992).
[9] P. Carra, B. T. Thole, M. Altarelli, and X. Wang, Phys. Rev. Lett. **70**, 694 (1993).
[10] H. A. Dürr, G. van der Laan, D. Spanke, F. U. Hillebrecht, and N. B. Brookes, Phys. Rev. B **56**, 8156 (1997).
[11] H. Ebert *et al.*, The Munich SPR-KKR package, Ver. 3.6, http://olymp.cup.uni-muenchen.de/ak/ebert/SPRKKR; H. Ebert, in *Electronic Structure and Physical Properties of Solids*, edited by H. Dreyssé, Lecture Notes in Physics Vol. 535 (Springer, Berlin), p. 191; H. Ebert, Rep. Prog. Phys. **59**, 1665 (1996).
[12] J. P. Perdew, K. Burke, and M. Ernzerhof, Phys. Rev. Lett. **77**, 3865 (1996).
[13] V. V. Sokolovskiy, V. D. Buchelnikov, M. A. Zagrebin, P. Entel, S. Sahoo, and M. Ogura, Phys. Rev. B **86**, 134418 (2012).
[14] K. Koepernik and H. Eschrig, Phys. Rev. B **59**, 1743 (1999); http://www.fplo.de.
[15] H. Eschrig, M. Richter, and I. Opahle, in *Relativistic Electronic Structure Theory-Part II: Applications*, edited by P. Schwerdtfeger (Elsevier, Amsterdam, 2004), p. 723.
[16] J. P. Perdew and Y. Wang, Phys. Rev. B **45**, 13244 (1992).
[17] J. Dubowik, Y. V. Kudryavtsev, and Y. P. Lee, J. Appl. Phys. **95**, 2912 (2004).
[18] G. Jakob, T. Eichhorn, M. Kallmayer, and H. J. Elmers, Phys. Rev. B **76**, 174407 (2007).
[19] N. D. Telling, P. S. Keatley, G. van der Laan, R. J. Hicken, E. Arenholz, Y. Sakuraba, M. Oogane, Y. Ando, K. Takanashi, A. Sakuma, and T. Miyazaki, Phys. Rev. B **78**, 184438 (2008).
[20] C. Antoniak, J. Lindner, M. Spasova, D. Sudfeld, M. Acet, M. Farle, K. Fauth, U. Wiedwald, H.-G. Boyen, P. Ziemann, F. Wilhelm, A. Rogalev, and S. Sun, Phys. Rev. Lett. **97**, 117201 (2006).
[21] S. Aksoy, T. Krenke, M. Acet, E. F. Wassermann, X. Moya, L. Mañosa, and A. Planes, Appl. Phys. Lett. **91**, 241916 (2007).
[22] S. R. Barman, S. Banik, and A. Chakrabarti, Phys. Rev. B **72**, 184410 (2005).
[23] P. Pörsch, M. Kallmayer, T. Eichhorn, G. Jakob, H. J. Elmers, C. A. Jenkins, C. Felser, R. Ramesh, and M. Huth, Appl. Phys. Lett. **93**, 022501 (2008).
[24] A. Auge, N. Teichert, M. Meinert, G. Reiss, A. Hütten, E. Yüzüak, I. Dincer, Y. Elerman, I. Ennen, and P. Schattschneider, Phys. Rev B **85**, 214118 (2012).
[25] M. E. Gruner, P. Entel, I. Opahle, and M. Richter, J. Mater. Sci. **43**, 3825 (2008).
[26] M. Siewert, M. E. Gruner, A. Hucht, H. C. Herper, A. Dannenberg, A. Chakrabarti, N. Singh, R. Arroyave, and P. Entel, Advanced Engineering Materials **14**, 530 (2012).